

Debiased Mapping for Full-Reference Image Quality Assessment

Baoliang Chen, Hanwei Zhu, liingyu Zhu, and Shiqi Wang, *Senior Member, IEEE*

Abstract—Mapping images to deep feature space for comparisons has been widely adopted in recent learning-based full-reference image quality assessment (FR-IQA) models. Analogous to the classical classification task, the ideal mapping space for quality regression should possess both inter-class separability and intra-class compactness. The inter-class separability that focuses on the discrimination of images with different quality levels has been highly emphasized in existing models. However, the intra-class compactness that maintains small objective quality variance of images with the same or indistinguishable quality escapes the research attention, potentially leading to the perception-biased measures. In this paper, we reveal that such bias is mainly caused by the unsuitable subspace that the features are projected and compared in. To account for this, we develop the Debiased Mapping based quality Measure (DMM), which relies on the orthonormal bases of deep learning features formed by singular value decomposition (SVD). The SVD in deep learning feature domain, which overwhelmingly separates the quality variations with singular values and projection bases, facilitates the quality inference with dedicatedly designed distance measure. Experiments on different IQA databases demonstrate the mapping method is able to efficiently mitigate the perception bias, and the superior performance on quality prediction verifies the effectiveness of our method. The implementation will be publicly available.

Index Terms—Image quality assessment, natural scene statistics, deep feature, weight distribution, nuclear norm.

1 INTRODUCTION

Given the reference image, the full-reference image quality assessment (FR-IQA) methods aim to automatically predict the quality score of a test image based on the fidelity/similarity between them. Typical FR-IQA models can be divided into two categories, *i.e.*, human visual system (HVS) inspired measures and data-driven measures. The former can be dated back to the 1970’s when a family of visual fidelity measures were explored for rate-distortion optimization [1]. The traditional error-sensitivity based methods attempt to map images to frequency domains by Fourier decomposition [1], Gabor decomposition [2], [3], local block discrete cosine transform [4] or wavelet transform [5], [6], based on the widely acknowledged principle that primary visual cortex presents different stimulus to different components. Inspired by the hypothesis that the HVS presents high sensitivity to the structural information, the structural similarity index (SSIM) was proposed in [7]. Though promising results have been achieved, the quality characterization capability is still limited by the hand-crafted features. To this end, data-driven measures have been widely studied in recent years. Zhang *et al.* revealed the unreasonable effectiveness of pre-trained convolutional neural network (CNN) representations for IQA [8]. Analogously, different distance measures for deep feature comparison were proposed, such as deep image structure and texture similarity (DISTS) [9], locally adaptive DISTS (A-DISTS) [10], and deep Wasser-

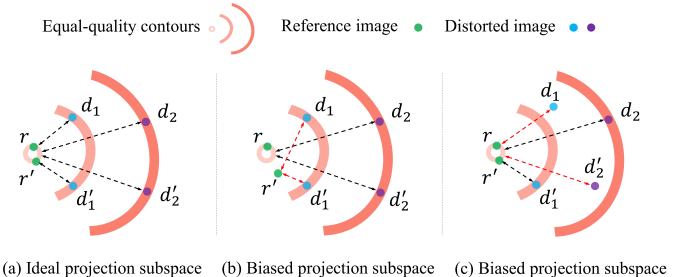


Fig. 1. Comparisons in different projection subspaces for FR-IQA. (a) Illustration of the ideal/unbiased projection, where images with indistinguishable quality (represented by points with the same color) are in the equal-quality contour. (b) Illustration of the biased projection caused by incoherent references, where there is a significant gap between the two pristine references r and r' . (c) Illustration of the biased projection caused by incoherent distorted images, such that the distances between the reference image and distorted images with the same visual quality (*e.g.*, d'_1 and d_1) are different.

stein distance (DeepWSD) [11]. In addition, several frameworks that learn the deep representations directly from labeled IQA data were proposed in [12], [13]. Despite the great success of those data-driven methods, herein, we would like to reveal the perception bias which still exists in the deep-feature space, hindering the reliable quality prediction.

As shown in Fig. 1(a), when images are projected into an ideal subspace for comparisons in quality inference, the images with the same quality (intra-class samples) are expected to lie on the equal-quality contour, and images with different quality (inter-class samples) are projected to different contours. In other words, the mapping subspace is desired to possess both intra-class compactness and inter-class separability. However, most deep-feature based models highlight the inter-class separability while neglecting the

• *B. Chen, H. Zhu, S. Wang, and S. Kwong are with the Department of Computer Science, City University of Hong Kong, Hong Kong. E-mail: blchen6-@my.cityu.edu.hk; huzhu4-c@my.cityu.edu.hk; lingyzhu-c@my.cityu.edu.hk; shiqwang@cityu.edu.hk, and cssamk@cityu.edu.hk.*

• *Corresponding author: Shiqi Wang.*

intra-class compactness. This could be further explained in Fig. 2, in which we present the perception bias that may exist in different scenarios. In particular, the feature misalignment in Figs. 2(a)~(d) which can be caused by local or global geometric transformations, deteriorates the intra-class compactness, as evidenced by the high coefficient of variation (CV) values in terms of different deep learning feature distance measures. In addition, as shown in Figs. 2(g)~(i), the similar level of quality degradation (as evidenced by the CV value of mean opinion scores (MOSSs)) can be caused by distortions in different feature components, such as orientation, intensity, and structure. However, existing quality measures in deep feature domain still fail to capture such compactness. In other words, without a proper projection decomposition, the feature distance measure could be sub-optimal, as it could overly stress one particular distortion type, potentially building up barriers against intra-class compactness.

In this paper, we propose the Debiased Mapping based Measure (DMM) with the principle of *exploring the responsible projection subspaces and defining effective distance measures within such subspaces*. The deep learning features, which could be accounted as the perceptual activations of particular patterns and concepts, can be further projected into subspaces formed by singular value decomposition (SVD). From the neuron activation perspective, the neuron output is treated as the explanation response of the particular pattern with neural networks. This motivates the SVD subspace representation of deep learning features, such that the statistical representations of activation responses with decreased importance can be utilized to mitigate the perception bias. On one hand, the singular values (SVs) from SVD enjoy the robustness of geometric transformations and are insensitive to small perturbations. On the other hand, the projection bases (PB) obtained by the SVD are orthogonal, such that the features could be mapped into several independent components for quality comparisons. The corresponding distance measure, base angle consistency, which characterizes the consistency of the angles between eigenvectors, further enhances the intra-class compactness, as evidenced by the results in Fig. 2 CV(DMM) and Section 4. The performance of DMM is evaluated on different IQA databases, and extensive experimental results have revealed its effectiveness.

2 RELATED WORK

2.1 FR-IQA Models

The classical per-pixel measure Peak Signal-to-Noise Ratio (PSNR) usually presents the poor consistency with HVS due to the assumption on per-pixel independence. In view of this, numerous alternative models were subsequently proposed. In [7], the structure similarity rather than the error visibility was measured in the SSIM index and this work was further extended to the multi-scale SSIM (MS-SSIM) [17], information content weighted SSIM (IW-SSIM) [18], and the complex wavelet SSIM (CW-SSIM) indices [19]. Based on the natural scene statistics, the information fidelity based models were proposed in information fidelity criterion (IFC) [20] and visual information fidelity (VIF) [21], with the assumption that higher mutual information results in better image quality. Recently,

perceptual comparisons in deep feature space dominate the FR-IQA research. Zhang *et al.* proposed the perceptual image patch similarity (LPIPS) index by measuring the Euclidean distance of the pre-trained VGG features [22]. Ding *et al.* presented the first DISTS metric with the global mean and variance of deep features [9]. They further extended the work to handle local structure and texture comparisons [10]. Liao *et al.* computed the deep feature distribution in wasserstein domain to capture the quality contamination rather than measuring the feature distance point-by-point [11]. In addition, models that learn the deep features from the human-rated data were also explored, such as deep IQA (DeepQA) model [23], weighted average deep image quality measure for FR-IQA (WaDIQaM-FR) [12], perceptual image-error assessment through pairwise preference (PieAPP) [13] and joint semi-supervised and positive-unlabeled learning (JSPL) [24]. However, due to the limited data, the learned models commonly encounter the overfitting problem when compared to the features derived from pre-trained networks.

2.2 Image Processing with SVD

Recent years have witnessed the successful applications of SVD in numerous image processing tasks. For example, an image can be compressed with acceptable quality by the truncated SVD transformation [25], [26], leading to significant storage savings. The SVD has also been widely utilized for noise signal filtering with the assumption that the SVD is able to project the noise into the subspace that is orthogonal to the data signal [27], [28]. The SV vector obtained by the SVD can be treated as a robust image representation due to its stability in the permutations caused by lighting conditions or rotations. For example, the normalized largest SV was adopted as the representation for face recognition in [29]. For image quality assessment, various SVD-based methods have been proposed. In [30], the content-dependent and content-independent components of an image are decomposed by the SVD for the design of component-specific distortion measures. Manish *et al.* learned a support vector regression for the aggregation of the SVD-based features [31]. The local SVD is adopted to extract the SV vectors and PB vectors for learning a quality prediction network [32]. However, those methods mainly apply the SVD in the pixel space and we make the first attempt to perform the SVD in the deep feature domain, facilitating the subspace generation for debiased perception.

3 METHODOLOGY

3.1 Preliminaries

Given a real rectangular matrix $\mathbf{A} \in \mathbb{R}^{m \times n}$ with its $\text{rank}(\mathbf{A}) = r$, the SVD decomposes \mathbf{A} into the product of three matrices: an orthogonal matrix \mathbf{U} , a diagonal matrix \mathbf{S} , and the transpose of an orthogonal matrix \mathbf{V} as follows,

$$\mathbf{A}_{m \times n} = \mathbf{U}_{m \times m} \cdot \mathbf{S}_{m \times n} \cdot \mathbf{V}^T_{n \times n}, \quad (1)$$

where

$$\begin{aligned} \mathbf{U} &= (\mathbf{u}_1, \mathbf{u}_2, \dots, \mathbf{u}_w, \dots, \mathbf{u}_m), \\ \mathbf{V} &= (\mathbf{v}_1, \mathbf{v}_2, \dots, \mathbf{v}_w, \dots, \mathbf{v}_n), \\ \mathbf{S} &= \text{diag}(\sigma_1, \sigma_2, \dots, \sigma_r, 0, \dots, 0). \end{aligned} \quad (2)$$

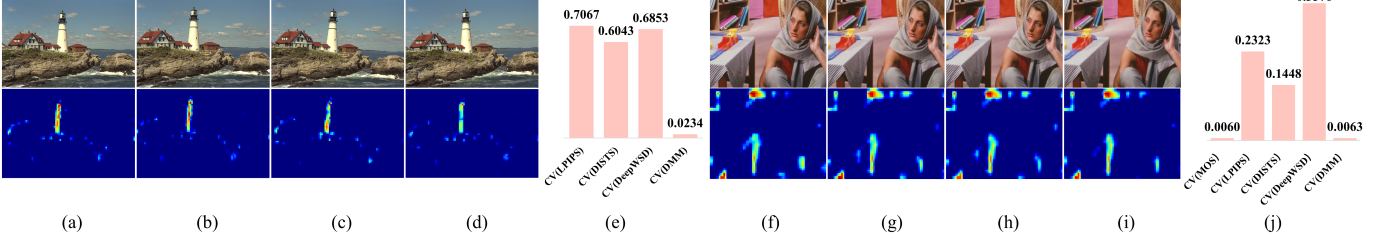


Fig. 2. Illustration of the perception bias caused by the violation of the intra-class compactness. (a) the reference image; (b) the distorted version of (a) with geometric transformations (scaling); (c) the distorted version of (a) with geometric transformations (rotation); (d) the distorted version of (a) with geometric transformations (scaling&rotation); (e) the CV of the quality scores from different FR-IQA methods (denoted as $CV(\cdot)$). It is worth mentioning that though the mild geometric distortions do not degrade the image quality, it is not surprising to find the relatively high CV values of LPIPS, DISTS, and DeepWSD. We also provide the toy example to illustrate this phenomenon in Fig. 1(b) when using these geometrically distorted images as the reference for quality inference. (f) the reference image; (g) the super-resolved image by first downsampling (f) with a factor of 3 then upsampling by [14]; (h) the super-resolved image by first downsampling (f) with a factor of 3 then upsampling by [15]; (i) the super-resolved image by first downsampling (f) with a factor of 2 then upsampling by [16]; (j) the CV of the MOSs and quality scores from different FR-IQA methods. The extremely low CV value of the MOSs of images (g)-(i) indicates the indistinguishable quality. Again, the relatively high CV values of LPIPS, DISTS, and DeepWSD reveal the unsatisfactory intra-class compactness of the three models. The toy example which illustrates this phenomenon is shown in Fig. 1(c), where equal-quality restored images are projected into the biased subspace with a large margin.

Herein, \mathbf{u} and \mathbf{v} are the left basis and right basis, respectively. σ is the SV with the descending order. The \mathbf{A} can also be expressed as $\mathbf{A} = \sum_{w=1}^r \sigma_w \mathbf{u}_w \mathbf{v}_w^T = \sigma_1 \mathbf{u}_1 \mathbf{v}_1^T + \sigma_2 \mathbf{u}_2 \mathbf{v}_2^T + \dots + \sigma_r \mathbf{u}_r \mathbf{v}_r^T$. It reveals the matrix \mathbf{A} is decomposed into a set of linearly independent components with SV as the energy contribution of each component. In particular, for the SV, we have: 1) $|\mathbf{A}\mathbf{A}^T - \sigma_w^2 \mathbf{I}| = |\mathbf{P}\mathbf{A}(\mathbf{P}\mathbf{A})^T - \sigma_w^2 \mathbf{I}| = 0$, where \mathbf{P} is an arbitrary unitary matrix. 2) $\|\mathbf{S}_A - \mathbf{S}_B\|_F \leq \|\mathbf{A} - \mathbf{B}\|_F$, where \mathbf{B} is another matrix sharing the same dimensions with \mathbf{A} and $\|\cdot\|_F$ is Frobenius norm. \mathbf{S}_A and \mathbf{S}_B are the SV vector of \mathbf{A} and \mathbf{B} , respectively. The former property reveals the SVs are invariant to the feature transposition, translation, and rotation [33] and the latter demonstrates the stability of SVs. For example, when \mathbf{B} is a small perturbation result of \mathbf{A} , the change of SVs can be bounded by the signal fidelity difference, resulting in the compactness when the SV vector is used to indicate quality-relevant representation.

3.2 Debiased Mapping For FR-IQA

Herein, we present the DMM FR-IQA method. First, quality-aware feature extraction is performed by the tailored VGG16 network. Subsequently, we capture the local distortion by performing SVD on the feature patches of each channel. In particular, For the SVs, we utilize the Euclidean distance to straightforwardly quantify the similarity. For the PB, an angle consistency measure is proposed, aiming to capture the destruction of the bases in a statistical way. Finally, the local distortion measure is further tuned with the global texture similarity adaptively, leading to the final quality measure.

Quality-aware Feature Extraction. Denoting the reference image as \mathbf{x} and the test image as \mathbf{y} , the aim of FR-IQA is to predict the image quality q of \mathbf{y} . Herein, instead of performing the SVD in the pixel space directly, the deep neural network pre-trained on ImageNet [34] is utilized for feature extraction due to its superior capability in capturing image distortions [8], [9], [11]. In particular, we select two layers of the VGG16 network [22] as the feature extractor. For simplification, we depict our model based on one layer

and the final measure is obtained based on both layers. Supposing the extractor of one layer is $\phi(\cdot)$, the feature extraction can be expressed as follows,

$$\mathbf{X} = \phi(\mathbf{x}), \mathbf{Y} = \phi(\mathbf{y}), \quad (3)$$

where $\mathbf{X}, \mathbf{Y} \in \mathbb{R}^{c \times h \times w}$. c is the channel number and the spatial size is denoted as (h, w) . As described before, the deep learning features \mathbf{X}, \mathbf{Y} are intrinsically bias, such that \mathbf{X}, \mathbf{Y} are re-projected to new subspaces by SVD.

Local Distortion Measure. In practice, the feature spatial size (h, w) can be various when the input image sizes are not fixed. To estimate the SVs stably, local patches with the same size $(k \times k)$ are sampled from the deep features successively. Then we perform the SVD on each of those patches to capture the local distortion (denoted as $\mathcal{D}_l(\mathbf{x}, \mathbf{y})$). In particular, the local distortion consists of both the distortion of SVs (denoted as $\mathcal{D}_l^s(\mathbf{x}, \mathbf{y})$) and the distortion of PB ($\mathcal{D}_l^b(\mathbf{x}, \mathbf{y})$) as follows,

$$\mathcal{D}_l(\mathbf{x}, \mathbf{y}) = \mathcal{D}_l^s(\mathbf{x}, \mathbf{y}) \cdot \mathcal{D}_l^b(\mathbf{x}, \mathbf{y}). \quad (4)$$

In detail, for $\mathcal{D}_l^s(\mathbf{x}, \mathbf{y})$, as we project the feature on orthogonal bases, the SVs in different bases are independent of each other, thus the point-wise comparison can be performed directly. Supposing there are n patches sampled from the feature map of each channel, the distance measure of SV (denoted as $\mathcal{D}_l^s(\mathbf{x}, \mathbf{y})$) is given by,

$$\mathcal{D}_l^s(\mathbf{x}, \mathbf{y}) = \frac{1}{nc} \sum_{i=1}^c \sum_{j=1}^n \|S_{\mathbf{X}_{i,j}} - S_{\mathbf{Y}_{i,j}}\|_2^2, \quad (5)$$

where $S_{\mathbf{X}_{i,j}}$ and $S_{\mathbf{Y}_{i,j}}$ are the vectors of SVs of $\mathbf{X}_{i,j}$ and $\mathbf{Y}_{i,j}$. i and j represent the channel and patch indices, respectively.

Regarding $\mathcal{D}_l^b(\mathbf{x}, \mathbf{y})$, a trivial way is to summarize each basis similarity by the vector angles. However, in IQA, we find the image quality is highly relevant to the angle consistency rather than angle values *i.e.* the variation of the angles is higher the PB distortion is severer. The reason may lie in that rotating each basis of the feature consistently can preserve the whole structure of the features while the inconsistent rotation deconstructs the feature structure and brings



Fig. 3. Four images generated by texture resampling (content of a texture region is replaced with new content sampled from an image with the same texture pattern). The local distortion can be inevitably introduced due to the misalignment caused by resampling, while the high global texture similarity leads to the indistinguishable quality. The images are sampled from TQD [9].

severe perceptual distortions. As such, we define the *basis angle consistency* to evaluate the distortion of the bases.

Definition 1 (Basis Angle Consistency). The CV value of the basis angle, where the basis angle means the angle between two singular vectors from reference/distorted images corresponding to the same SV index.

Herein, we use the cosine similarity to represent the basis angle and measure its consistency (denoted as $\mathcal{D}_l^b(\mathbf{x}, \mathbf{y})$) as follows,

$$\mathcal{D}_l^b(\mathbf{x}, \mathbf{y}) = \frac{1}{nc} \sum_{i=1}^c \sum_{j=1}^n \left(\frac{\sigma_{i,j}^\theta}{\mu_{i,j}^\theta + \tau_1} \right), \quad (6)$$

where τ_1 is a small positive constant to avoid dividing by zero. The $\mu_{i,j}^\theta$ and $\sigma_{i,j}^\theta$ capture the statistics of the angles $\theta_{i,j,t}$, which are defined as follows,

$$\mu_{i,j}^\theta = \frac{1}{k} \sum_{t=1}^k |\cos(\theta_{i,j,t})|, \quad (7)$$

$$\sigma_{i,j}^\theta = \sqrt{\frac{1}{k-1} \sum_{t=1}^k \left(|\cos(\theta_{i,j,t})| - \mu_{i,j}^\theta \right)^2}, \quad (8)$$

where

$$\cos(\theta_{i,j,t}) = \frac{\langle \mathbf{u}_{\mathbf{X}_{i,j}}^t, \mathbf{u}_{\mathbf{Y}_{i,j}}^t \rangle}{\| \mathbf{u}_{\mathbf{X}_{i,j}}^t \| \| \mathbf{u}_{\mathbf{Y}_{i,j}}^t \|}. \quad (9)$$

Herein, $\mathbf{u}_{\mathbf{X}_{i,j}}^t$ is the t -th eigenvector in $\mathbf{U}_{\mathbf{X}_{i,j}}$, corresponding to the t -th largest SV in $\mathbf{X}_{i,j}$. Moreover, $\mathbf{u}_{\mathbf{Y}_{i,j}}^t$ from image \mathbf{y} is extracted in a similar way.

Aggregation Oriented Tuning. The top-down visual perception philosophy of HVS reveals that local distortion aggregation is usually affected by global texture similarity. A typical example is shown in Fig. 3, in which four texture-resampled images are of indistinguishable quality, while a large variance can be observed in patches corresponding to

the same location. This phenomenon inspires us to introduce the local distortion tuning term by the global texture similarity as follows,

$$\mathcal{D}_g(\mathbf{x}, \mathbf{y}) = \exp(-\alpha \mathcal{S}_g(\mathbf{x}, \mathbf{y})), \quad (10)$$

where the $\mathcal{S}_g(\mathbf{x}, \mathbf{y})$ is the global texture similarity defined by,

$$\mathcal{S}_g(\mathbf{x}, \mathbf{y}) = \frac{1}{c} \sum_{i=1}^c \frac{2\mu_{\mathbf{X}_i} \mu_{\mathbf{Y}_i} + \tau_2}{(\mu_{\mathbf{X}_i})^2 + (\mu_{\mathbf{Y}_i})^2 + \tau_3}, \quad (11)$$

and the $\mu_{\mathbf{X}_i}$ and $\mu_{\mathbf{Y}_i}$ are the global means of \mathbf{X}_i and \mathbf{Y}_i , respectively. Two small positive constants, τ_2 and τ_3 , are included to avoid the denominators being zero. Moreover, α is a hyper-parameters to adjust the weight sensitivities. In summary, the final quality measure DMM is defined as follows,

$$\mathcal{D}(\mathbf{x}, \mathbf{y}) = \mathcal{D}_g(\mathbf{x}, \mathbf{y}) \cdot \mathcal{D}_l(\mathbf{x}, \mathbf{y}) \quad (12)$$

$$= \mathcal{D}_g(\mathbf{x}, \mathbf{y}) \cdot \mathcal{D}_l^s(\mathbf{x}, \mathbf{y}) \cdot \mathcal{D}_l^b(\mathbf{x}, \mathbf{y}). \quad (13)$$

It is worth noting that the DMM is an *opinion-unaware* model, *i.e.*, the model is independent of the testing data. This advantage suggests that the DMM is a more generalized IQA measure rather than over-fitting to a specific dataset.

4 EXPERIMENT

In this section, we first describe our implementation details, then the experiments on both synthetically distorted images and restored images are conducted. To verify the enhanced intra-class compactness, we further propose a retrieval task of image pairs with min-max perception distance. Finally, the ablation studies are performed to reveal the functionality of each module.

4.1 Implementation Details

We implement our model by PyTorch [43]. Two layers of VGG16 network are utilized for the feature extraction, including the “ReLU3_3” layer and “ReLU4_3” layer. Supposing the shorter side of the input image is h , we resize it to $\max(\lfloor \frac{h}{48} \rfloor \times 32, 128)$ by maintaining the aspect ratio. In Eqns. (6) and (11), we set $\tau_1 = \tau_2 = \tau_3 = 1e-6$. The α in Eqn. (10) is set to 2.0 and the patch size k is 16 with a stride size of 4. Two evaluation metrics are reported for each experimental setting, including the Spearman’s rank correlation coefficient (SRCC) and Pearson linear correlation coefficient (PLCC). In particular, the PLCC evaluates the prediction accuracy and the SRCC indicates the prediction monotonicity. We map the predicted scores to the MOSs with a five-parameter nonlinear logistic function [44] when computing PLCC. The performance is evaluated on six IQA datasets, including the TID2013 [45], LIVE [20], CSIQ [39], KADID-10k [46], PIPAL [47] and QADS [48]. In particular, the first four datasets consist of synthetically distorted images with the number of images ranging from 982 to 10,125. To our best knowledge, the PIPAL dataset is the largest IQA dataset. It contains 29k images in total and each reference image has 116 distortions, including the Generative Adversarial Network (GAN) generated images. The QADS dataset is designed especially for the quality assessment of super-resolved images (SRIs). It contains 20 high-resolution images and 980 SRIs generated by 21 different SR methods.

Method	LIVE		CSIQ		TID2013		KADID-10k		PIPAL	
	SRCC	PLCC								
PSNR	0.873	0.868	0.809	0.815	0.688	0.679	0.676	0.680	0.407	0.415
SSIM [7]	0.931	0.928	0.872	0.868	0.720	0.745	0.724	0.723	0.498	0.505
MS-SSIM [17]	0.931	0.931	0.908	0.896	0.798	0.810	0.802	0.801	0.552	0.590
VIF [21]	0.927	0.925	0.902	0.887	0.690	0.732	0.593	0.602	0.443	0.468
FSIM [35]	0.965	0.961	0.931	0.919	0.851	0.877	0.854	0.851	0.589	0.615
NLPD [36]	0.914	0.914	0.917	0.911	0.808	0.823	0.810	0.810	0.469	0.509
Style [37]	0.898	0.882	0.853	0.837	0.675	0.681	0.701	0.707	0.339	0.337
PieAPP [13]	0.908	0.919	0.877	0.892	0.850	0.848	0.836	0.836	0.700	0.712
LPIPS [8]	0.932	0.934	0.883	0.906	0.694	0.759	0.720	0.729	0.573	0.611
DISTS [9]	0.954	0.954	0.939	0.941	0.830	0.856	0.887	0.886	0.623	0.644
DSD [38]	0.577	0.552	0.603	0.700	0.548	0.657	0.439	0.527	0.274	0.350
DeepWSD [11]	0.952	0.949	0.954	0.947	0.869	0.893	0.881	0.880	0.574	0.583
DMM	0.946	0.928	0.954	0.937	0.876	0.892	0.918	0.914	0.710	0.731

TABLE 1
Performance comparison of DMM against twelve FR-IQA models. The best two results are highlighted in boldface.

Method	PSNR	SSIM [7]	MS-SSIM [17]	VIF [21]	MAD [39]	IW-SSIM [18]	IGM [40]
SRCC	0.354	0.529	0.717	0.815	0.723	0.820	0.715
PLCC	0.390	0.533	0.724	0.821	0.731	0.823	0.719
Method	FSIM [35]	GMSD [41]	DASM [42]	LPIPS [8]	DeepWSD [11]	DISTS [9]	DMM
SRCC	0.689	0.765	0.751	0.671	0.758	0.809	0.862
PLCC	0.690	0.775	0.759	0.673	0.770	0.808	0.868

TABLE 2
Performance comparison on QADS dataset. The best two results are highlighted in boldface.

4.2 Performance on Synthetically Distorted Images

We first compare our method on the TID2013, LIVE, CSIQ, KADID-10k, and PIPAL datasets, in which most images are synthetically distorted. We compare DMM with 12 FR-IQA models, including the traditional models: PSNR, SSIM [7], MS-SSIM [17], VIF [21], feature similarity (FSIM) index [35], normalised Laplacian pyramid distance (NLPD) [36], and deep-learning based IQA models: Style [37], PieAPP [13], LPIPS [8], DISTS [9], deep self dissimilarity (DSD) [38] and DeepWSD [11]. In particular, the PieAPP and LPIPS are trained on the PIPAL dataset and BAPPS dataset [8], respectively. The DISTS is tuned on both the KADID-10k [46] dataset and DTD dataset [49]. The DSD, DeepWSD, and our method DMM are based on the pre-trained VGG network without any IQA dataset involved in training.

The comparison results are presented in Table 1, from which we can observe the proposed DMM achieves superior performance on three traditional datasets (*i.e.*, LIVE, CSIQ, and TID2013) and two large-scale datasets (*i.e.*, KADID-10k and PIPAL). The tradition FR-IQA models may overfit to small-scale IQA datasets (*e.g.*, LIVE and CSIQ) and perform worse on large-scale datasets. Moreover, the majority of IQA models show poor correlation with human perception for the PIPAL dataset because of the diverse and complicated distortions. By contrast, the proposed DMM still achieves the best performance. We believe the performance gain mainly originates from the debiased deep feature mapping

and opinion-unaware learning.

Method	PIPAL (GAN distortion)	
	SRCC	PLCC
SSIM [7]	0.322	0.472
MS-SSIM [17]	0.387	0.615
VIF [21]	0.324	0.543
FSIM [35]	0.410	0.621
NLPD [36]	0.341	0.570
LPIPS [8]	0.486	0.617
PieAPP [13]	0.553	0.632
DISTS [9]	0.549	0.607
DeepWSD [11]	0.397	0.560
FID [50]	0.413	0.496
DMM	0.604	0.715

TABLE 3
Performance comparison on the GAN distorted images from the PIPAL. The best two results are highlighted in boldface.

4.3 Performance on Restored Images

In addition to the synthetically distorted images, the distortions, such as the appealing texture and geometric distortion introduced by the image restoration methods, cast a grand

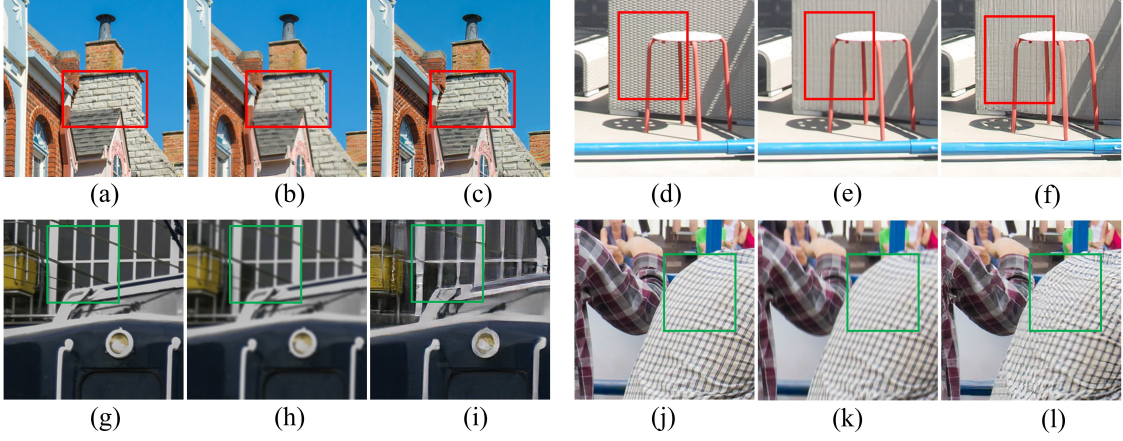


Fig. 4. Illustration of the restored images in the PIPAL dataset. (a), (d), (g), and (j) are the reference images; (c), (f), (i), and (l) are the GAN-generated images; (b), (e), (h), and (k) are images sampled for comparison with a lower quality (smaller MOS values) than (c), (f), (i), and (l), and the distortion types included both synthetic distortion and GAN distortion. Comparison regions with appealing textures and geometric transformation are highlighted by the red rectangles and green rectangles, respectively. Existing quality measures including LPIPS, DISTs, and DeepWSD show opposite quality preference with the MOS on each image pair (e.g. a higher quality score is predicted for (b) than (c) by LPIPS), while the preference of our method is always consistent with the MOS in each pair.

Method	LPIPS [8]	DISTS [9]	DeepWSD [11]	DMM
$ \Delta \text{MOS} $	0.1287	0.0818	0.0768	0.0484

TABLE 4

The average of absolute MOS difference of pairs (with minimum quality difference) retrieved with different quality measures.

challenge to existing FR-IQA measures. To this end, we further validate the proposed model on the SR-resolved images including the QADS dataset and the GAN-generated images in the PIPAL dataset. The results are shown in Table 2 and Table 3, respectively. We can observe that DMM outperforms the compared measures by a significant margin for both SR-resolved and GAN-generated images. We also provide the samples in Fig. 4, from which we can see that the proposed method presents high consistency with the MOSs, as the projected SVs enhance the robustness of our model in the misalignment scenarios and the orthogonal decomposition leads to a more reliable subspace for feature comparison. However, the complicated distortion types create the daunting challenges to the existing models, even the reference and distorted images are compared in the deep learning feature domain.

4.4 Application on Image Pairs Retrieval

In this subsection, we design a new experiment to demonstrate the capability of FR-IQA models in pursuing inter-class separability and intra-class compactness. Assuming there are η distorted images sharing the same reference image, in total there are $\eta(\eta - 1)/2$ pairs formed by these distorted images. Given a FR-IQA model, the absolute quality score difference within each pair can thus be obtained, and the pairs with the minimum and maximum quality differences are finally selected. Ideally, the MOS difference between two images in a pair shall be in line with the difference in terms of IQA scores. We conduct the experiments on the QADS dataset and visualize the retrieval results in Fig. 5. From the figure, we can observe that most of the

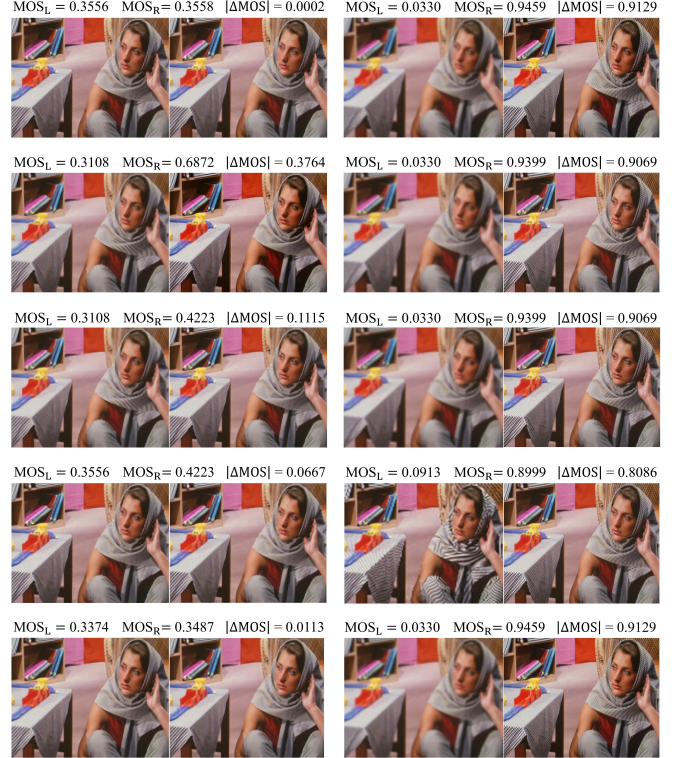


Fig. 5. Illustration of retrieved image pairs. Left: the pairs with minimum quality differences. Right: the pairs with maximum quality differences. The measures utilized in each row (from top to down) are the MOS, LPIPS, DISTs, DeepWSD, and our DMM.

IQA measures can retrieve the discriminative image pairs with a large perception gap in terms of MOS scores, while they usually fail in the retrieval of image pairs with similar quality levels. By contrast, the proposed DMM is promising for the retrieved pairs with both minimum and maximum differences. Moreover, we average the absolute MOS difference of pairs (with minimum quality difference) retrieved with different quality measures. The results are shown in Table 4, and the smallest value enjoyed by DMM further

Backbone	Layer	TID2013	KADID-10k	PIPAL	QADS	LIVE	CSIQ	Mean
VGG16	ReLU1_2	0.828	0.870	0.655	0.741	0.881	0.901	0.813
	ReLU2_2	0.859	0.908	0.701	0.816	0.917	0.938	0.856
	ReLU3_3	0.876	0.918	0.712	0.864	0.939	0.948	0.876
	ReLU4_3	0.868	0.905	0.692	0.838	0.956	0.953	0.869
	ReLU5_3	0.844	0.864	0.616	0.767	0.936	0.913	0.823
	ReLU3_3&4_3	0.876	0.919	0.710	0.862	0.946	0.954	0.878
VGG19	ReLU1_2	0.824	0.868	0.656	0.747	0.878	0.899	0.812
	ReLU2_2	0.860	0.907	0.699	0.810	0.921	0.941	0.856
	ReLU3_4	0.832	0.870	0.675	0.861	0.935	0.933	0.851
	ReLU4_4	0.864	0.907	0.684	0.816	0.961	0.951	0.864
ResNet50	Layer_2	0.877	0.836	0.650	0.812	0.877	0.872	0.821
	Layer_3	0.901	0.830	0.627	0.771	0.901	0.887	0.820
DenseNet121	DenseBlock_2	0.800	0.797	0.474	0.675	0.892	0.891	0.755
	DenseBlock_3	0.821	0.793	0.494	0.695	0.913	0.886	0.767

TABLE 5

SRCC comparison results of different feature extractors. The best two results are highlighted in boldface. The default setting of DMM is highlighted.

Exp. ID	\mathcal{D}_l^s	\mathcal{D}_l^b	\mathcal{D}_g	TID2013	KADID-10k	PIPAL	QADS	LIVE	CSIQ	Mean
1	✓	✗	✗	0.873	0.882	0.694	0.834	0.945	0.952	0.863
2	✗	✓	✗	0.773	0.785	0.619	0.769	0.916	0.924	0.798
3	✗	✗	✓	0.825	0.906	0.671	0.846	0.948	0.920	0.853
4	✓	✗	✓	0.873	0.909	0.700	0.855	0.946	0.949	0.872
5	✗	✓	✓	0.792	0.830	0.668	0.855	0.944	0.943	0.839
6	✓	✓	✗	0.876	0.917	0.706	0.852	0.945	0.957	0.875
7	✓	✓	✓	0.876	0.919	0.710	0.862	0.946	0.954	0.878

TABLE 6
SRCC results on different combinations of \mathcal{D}_l^s , \mathcal{D}_l^b and \mathcal{D}_g . The best two results are highlighted in boldface.

demonstrates the capability in maintaining high intra-class compactness.

4.5 Ablation Studies

In our method, the ‘ReLU3_3’ and ‘ReLU4_3’ layers of the VGG16 network are selected as the feature extractor. To explore other possible settings, we first explore the performance of other possible layers of the VGG16, then different backbones are studied, including the VGG19, ResNet50 [51], and DenseNet121 [52]. All those backbones are pre-trained on the ImageNet dataset. The results are shown in Table 5, from which we can observe the most effective layers are in the middle. The reason may lie in that the features extracted in the shallower layers are not abstract enough for quality-aware feature extraction and the features obtained by deeper layers may not be sensitive to quality distortion as high-level semantic features are learned. Moreover, the backbones also affect the performance significantly and the best backbone is the VGG16 network.

As shown in Table 6, we investigate the effectiveness of \mathcal{D}_l^s , \mathcal{D}_l^b and \mathcal{D}_g by providing the results with different combinations. First, we isolate each component and evaluate the performance on six IQA datasets individually. From the results of experiments 1~3, we can observe that each of them shows a certain extent of consistency with human

ratings, revealing all three terms are able to capture the distortion. Then we ablate each one from our model and design three experiments 4~6. The results show that all three types of ablation witness the performance drop, demonstrating they all contribute to the final results. In particular, compared with the default setting, the ablation of SV distortion measure \mathcal{D}_l^s leads to a dramatic performance drop on both systemically distorted images (e.g. SRCC 0.792 vs. 0.876 on the TID2013 dataset) and restored images (e.g. SRCC 0.668 vs. 0.710 on the PIPAL dataset). This phenomenon indicates the generalization capability of SVs for capturing images with different distortions. In addition, as shown in experiment 6, the ablation of \mathcal{D}_g brings a negative effect, especially on the QADS dataset (SRCC 0.852 vs. 0.862), revealing the importance of the global information for quality assessment of restored images. The best performance is achieved when all three terms are adopted, demonstrating the complementary functionalities of \mathcal{D}_l^s , \mathcal{D}_l^b , and \mathcal{D}_g .

5 CONCLUSION

This paper explores the debiased mapping for FR-IQA, from the perspective of SVD subspaces projection in the deep feature domain. We have developed the DMM model which effectively quantifies the visual quality, and maintains the intra-class compactness via the orthogonal decomposition.

Extensive experimental results show that the proposed model is effective on both synthetic distortions and distortions caused by restoring models. The enhancement of intra-class compactness yields the significant performance gain for both image quality prediction and quality-aware image retrieval.

APPENDIX A PROOF OF THE FIRST ZONKLAR EQUATION

Appendix one text goes here.

APPENDIX B

Appendix two text goes here.

REFERENCES

- [1] J. Mannos and D. Sakrison, "The effects of a visual fidelity criterion of the encoding of images," *IEEE Transactions on Information Theory*, vol. 20, no. 4, pp. 525–536, 1974. [1](#)
- [2] K. R. Nielsen, A. B. Watson, and A. J. Ahumada, "Application of a computable model of human spatial vision to phase discrimination," *Journal of the Optical Society of America A*, vol. 2, no. 9, pp. 1600–1606, 1985. [1](#)
- [3] C. C. Taylor, Z. Pizlo, J. P. Allebach, and C. A. Bouman, "Image quality assessment with a Gabor pyramid model of the human visual system," in *Human Vision and Electronic Imaging II*, 1997, pp. 58–69. [1](#)
- [4] A. B. Watson, "DCTune: A technique for visual optimization of DCT quantization matrices for individual images," in *Sid International Symposium Digest of Technical Papers*, 1993, pp. 946–946. [1](#)
- [5] Y.-K. Lai and C.-C. J. Kuo, "A haar wavelet approach to compressed image quality measurement," *Journal of Visual Communication and Image Representation*, vol. 11, no. 1, pp. 17–40, 2000. [1](#)
- [6] A. B. Watson, G. Y. Yang, J. A. Solomon, and J. Villasenor, "Visibility of wavelet quantization noise," *IEEE Transactions on Image Processing*, vol. 6, no. 8, pp. 1164–1175, 1997. [1](#)
- [7] Z. Wang, A. C. Bovik, H. R. Sheikh, and E. P. Simoncelli, "Image quality assessment: From error visibility to structural similarity," *IEEE Transactions on Image Processing*, vol. 13, no. 4, pp. 600–612, 2004. [1, 2, 5](#)
- [8] R. Zhang, P. Isola, A. A. Efros, E. Shechtman, and O. Wang, "The unreasonable effectiveness of deep features as a perceptual metric," in *IEEE Conference on Computer Vision and Pattern Recognition*, 2018, pp. 586–595. [1, 3, 5, 6](#)
- [9] K. Ding, K. Ma, S. Wang, and E. P. Simoncelli, "Image quality assessment: Unifying structure and texture similarity," *IEEE Transactions on Pattern Analysis and Machine Intelligence*, vol. 44, no. 5, pp. 2567–2581, 2020. [1, 2, 3, 4, 5, 6](#)
- [10] K. Ding, Y. Liu, X. Zou, S. Wang, and K. Ma, "Locally adaptive structure and texture similarity for image quality assessment," in *ACM International Conference on Multimedia*, 2021, pp. 2483–2491. [1, 2](#)
- [11] X. Liao, B. Chen, H. Zhu, S. Wang, M. Zhou, and S. Kwong, "DeepWSD: Projecting degradations in perceptual space to wasserstein distance in deep feature space," in *ACM International Conference on Multimedia*, 2022. [1, 2, 3, 5, 6](#)
- [12] S. Bosse, D. Maniry, K.-R. Müller, T. Wiegand, and W. Samek, "Deep neural networks for no-reference and full-reference image quality assessment," *IEEE Transactions on Image Processing*, vol. 27, no. 1, pp. 206–219, 2017. [1, 2](#)
- [13] E. Prashnani, H. Cai, Y. Mostofi, and P. Sen, "PieAPP: Perceptual image-error assessment through pairwise preference," in *IEEE Conference on Computer Vision and Pattern Recognition*, 2018, pp. 1808–1817. [1, 2, 5](#)
- [14] K. I. Kim and Y. Kwon, "Single-image super-resolution using sparse regression and natural image prior," *IEEE Transactions on Pattern Analysis and Machine Intelligence*, vol. 32, no. 6, pp. 1127–1133, 2010. [3](#)
- [15] W. T. Freeman, T. R. Jones, and E. C. Pasztor, "Example-based super-resolution," *IEEE Computer Graphics and Applications*, vol. 22, no. 2, pp. 56–65, 2002. [3](#)
- [16] J.-B. Huang, A. Singh, and N. Ahuja, "Single image super-resolution from transformed self-exemplars," in *IEEE Conference on Computer Vision and Pattern Recognition*, 2015, pp. 5197–5206. [3](#)
- [17] Z. Wang, E. P. Simoncelli, and A. C. Bovik, "Multiscale structural similarity for image quality assessment," in *Asilomar Conference on Signals, Systems & Computers*, 2003, pp. 1398–1402. [2, 5](#)
- [18] Z. Wang and Q. Li, "Information content weighting for perceptual image quality assessment," *IEEE Transactions on Image Processing*, vol. 20, no. 5, pp. 1185–1198, 2010. [2, 5](#)
- [19] Z. Wang and E. P. Simoncelli, "Translation insensitive image similarity in complex wavelet domain," in *IEEE International Conference on Acoustics, Speech, and Signal Processing*, 2005, pp. 573–576. [2](#)
- [20] H. R. Sheikh, Z. Wang, L. Cormack, and A. C. Bovik, "Image and video quality assessment research at LIVE," 2006. [Online]. Available: <https://live.ece.utexas.edu/research/Quality/subjective.htm> [2, 4](#)
- [21] H. R. Sheikh and A. C. Bovik, "Image information and visual quality," *IEEE Transactions on Image Processing*, vol. 15, no. 2, pp. 430–444, 2006. [2, 5](#)
- [22] K. Simonyan and A. Zisserman, "Very deep convolutional networks for large-scale image recognition," in *International Conference on Learning Representations*, 2015, pp. 1–6. [2, 3](#)
- [23] J. Kim and S. Lee, "Deep learning of human visual sensitivity in image quality assessment framework," in *IEEE Conference on Computer Vision and Pattern Recognition*, 2017, pp. 1676–1684. [2](#)
- [24] Y. Cao, Z. Wan, D. Ren, Z. Yan, and W. Zuo, "Incorporating semi-supervised and positive-unlabeled learning for boosting full reference image quality assessment," in *IEEE Conference on Computer Vision and Pattern Recognition*, 2022, pp. 5851–5861. [2](#)
- [25] J.-F. Yang and C.-L. Lu, "Combined techniques of singular value decomposition and vector quantization for image coding," *IEEE Transactions on Image Processing*, vol. 4, no. 8, pp. 1141–1146, 1995. [2](#)
- [26] R. Kakarala and P. O. Ogunbona, "Signal analysis using a multiresolution form of the singular value decomposition," *IEEE Transactions on Image processing*, vol. 10, no. 5, pp. 724–735, 2001. [2](#)
- [27] K. Konstantinides, B. Natarajan, and G. S. Yovanof, "Noise estimation and filtering using block-based singular value decomposition," *IEEE transactions on image processing*, vol. 6, no. 3, pp. 479–483, 1997. [2](#)
- [28] H. Prasantha, H. Shashidhara, and K. B. Murthy, "Image compression using SVD," in *International Conference on Computational Intelligence and Multimedia Applications*, 2007, pp. 143–145. [2](#)
- [29] W. Kim, S. Suh, W. Hwang, and J.-J. Han, "SVD face: Illumination-invariant face representation," *IEEE Signal Processing Letters*, vol. 21, no. 11, pp. 1336–1340, 2014. [2](#)
- [30] S. Wang, C. Deng, W. Lin, B. Zhao, and J. Chen, "A novel SVD-based image quality assessment metric," in *IEEE International Conference on Image Processing*, 2013, pp. 423–426. [2](#)
- [31] M. Narwaria and W. Lin, "SVD-based quality metric for image and video using machine learning," *IEEE Transactions on Systems, Man, and Cybernetics, Part B*, vol. 42, no. 2, pp. 347–364, 2011. [2](#)
- [32] A. Hu, R. Zhang, D. Yin, and Y. Zhan, "Image quality assessment using a SVD-based structural projection," *Signal Processing: Image Communication*, vol. 29, no. 3, pp. 293–302, 2014. [2](#)
- [33] Z.-Q. Hong, "Algebraic feature extraction of image for recognition," *Pattern Recognition*, vol. 24, no. 3, pp. 211–219, 1991. [3](#)
- [34] J. Deng, W. Dong, R. Socher, L.-J. Li, K. Li, and L. Fei-Fei, "ImageNet: A large-scale hierarchical image database," in *IEEE Conference on Computer Vision and Pattern Recognition*, 2009, pp. 248–255. [3](#)
- [35] L. Zhang, L. Zhang, X. Mou, and D. Zhang, "FSIM: A feature similarity index for image quality assessment," *IEEE Transactions on Image Processing*, vol. 20, no. 8, pp. 2378–2386, 2011. [5](#)
- [36] V. Laparra, J. Ballé, A. Berardino, and E. P. Simoncelli, "Perceptual image quality assessment using a normalized laplacian pyramid," *Electronic Imaging*, vol. 2016, no. 16, pp. 1–6, 2016. [5](#)
- [37] L. A. Gatys, A. S. Ecker, and M. Bethge, "Image style transfer using convolutional neural networks," in *IEEE Conference on Computer Vision and Pattern Recognition*, 2016, pp. 2414–2423. [5](#)
- [38] I. Kligvasser, T. Shaham, Y. Bahat, and T. Michaeli, "Deep self-dissimilarities as powerful visual fingerprints," in *Neural Information Processing Systems*, 2021, pp. 3939–3951. [5](#)
- [39] E. C. Larson and D. M. Chandler, "Most apparent distortion: Full-reference image quality assessment and the role of strategy," *Journal of Electronic Imaging*, vol. 19, no. 1, pp. 1–21, 2010. [4, 5](#)

[40] J. Wu, W. Lin, G. Shi, and A. Liu, "Perceptual quality metric with internal generative mechanism," *IEEE Transactions on Image Processing*, vol. 22, no. 1, pp. 43–54, 2012. [5](#)

[41] W. Xue, L. Zhang, X. Mou, and A. C. Bovik, "Gradient magnitude similarity deviation: A highly efficient perceptual image quality index," *IEEE Transactions on Image Processing*, vol. 23, no. 2, pp. 684–695, 2013. [5](#)

[42] L. Ding, H. Huang, and Y. Zang, "Image quality assessment using directional anisotropy structure measurement," *IEEE Transactions on Image Processing*, vol. 26, no. 4, pp. 1799–1809, 2017. [5](#)

[43] A. Paszke, S. Gross, F. Massa, A. Lerer, J. Bradbury, G. Chanan, T. Killeen, Z. Lin, N. Gimelshein, L. Antiga *et al.*, "PyTorch: An imperative style, high-performance deep learning library," in *Neural Information Processing Systems*, 2019, pp. 8026–8037. [4](#)

[44] VQEG, "Final report from the video quality experts group on the validation of objective models of video quality assessment," 2000. [Online]. Available: <http://www.vqeg.org> [4](#)

[45] N. Ponomarenko, L. Jin, O. Ieremeiev, V. Lukin, K. Egiazarian, J. Astola, B. Vozel, K. Chehdi, M. Carli, F. Battisti *et al.*, "Image database TID2013: Peculiarities, results and perspectives," *Signal Processing: Image Communication*, vol. 30, pp. 57–77, 2015. [4](#)

[46] H. Lin, V. Hosu, and D. Saupe, "KADID-10k: A large-scale artificially distorted IQA database," in *International Conference on Quality of Multimedia Experience*, 2019, pp. 1–3. [4, 5](#)

[47] G. Jinjin, C. Haoming, C. Haoyu, Y. Xiaoxing, J. S. Ren, and D. Chao, "PIPAL: A large-scale image quality assessment dataset for perceptual image restoration," in *European Conference on Computer Vision*, 2020, pp. 633–651. [4](#)

[48] F. Zhou, R. Yao, B. Liu, and G. Qiu, "Visual quality assessment for super-resolved images: Database and method," *IEEE Transactions on Image Processing*, vol. 28, no. 7, pp. 3528–3541, 2019. [4](#)

[49] M. Cimpoi, S. Maji, I. Kokkinos, S. Mohamed, and A. Vedaldi, "Describing textures in the wild," in *IEEE Conference on Computer Vision and Pattern Recognition*, 2014, pp. 3606–3613. [5](#)

[50] M. Heusel, H. Ramsauer, T. Unterthiner, B. Nessler, and S. Hochreiter, "GANs trained by a two time-scale update rule converge to a local nash equilibrium," in *Neural Information Processing Systems*, 2017, pp. 1–9. [5](#)

[51] K. He, X. Zhang, S. Ren, and J. Sun, "Deep residual learning for image recognition," in *IEEE Conference on Computer Vision and Pattern Recognition*, 2016, pp. 770–778. [7](#)

[52] G. Huang, Z. Liu, L. Van Der Maaten, and K. Q. Weinberger, "Densely connected convolutional networks," in *IEEE Conference on Computer Vision and Pattern Recognition*, 2017, pp. 4700–4708. [7](#)